Monthly Notices
of the
ROYAL ASTRONOMICAL SOCIETY

MNRAS **489,** 594–607 (2019)
Advance Access publication 2019 July 31
doi:10.1093/mnras/stz2086

Elemental and molecular abundances in comet 67P/Churyumov-Gerasimenko

Martin Rubin,[1★] Kathrin Altwegg,[1] Hans Balsiger,[1] Jean-Jacques Berthelier,[2] Michael R. Combi,[3] Johan De Keyser,[4] Maria Drozdovskaya,[5] Björn Fiethe,[6] Stephen A. Fuselier,[7,8] Sébastien Gasc,[1] Tamas I. Gombosi,[3] Nora Hänni,[1] Kenneth C. Hansen,[3] Urs Mall,[9] Henri Rème,[10] Isaac R. H. G. Schroeder,[1] Markus Schuhmann,[1] Thierry Sémon,[1] Jack H. Waite,[7] Susanne F. Wampfler[5] and Peter Wurz[1,5]

[1] *Physikalisches Institut, University of Bern, Sidlerstrasse 5, CH-3012 Bern, Switzerland*
[2] *Laboratoire Atmosphères, Milieux, Observations Spatiales, Institut Pierre Simon Laplace, CNRS, Université Pierre et Marie Curie, 4 Avenue de Neptune, F-94100 Saint-Maur, France*
[3] *Department of Climate and Space Sciences and Engineering, University of Michigan, 2455 Hayward, Ann Arbor, MI 48109, USA*
[4] *Koninklijk Belgisch Instituut voor Ruimte-Aeronomie – Institut Royal Belge d'Aéronomie Spatiale, Ringlaan 3, B-1180 Brussels, Belgium*
[5] *Center for Space and Habitability, University of Bern, Gesellschaftsstrasse 6, CH-3012 Bern, Switzerland*
[6] *Institute of Computer and Network Engineering (IDA), TU Braunschweig, Hans-Sommer-Straße 66, D-38106 Braunschweig, Germany*
[7] *Space Science Directorate, Southwest Research Institute, 6220 Culebra Rd., San Antonio, TX 78228, USA*
[8] *University of Texas at San Antonio, San Antonio, TX 78249, USA*
[9] *Max-Planck-Institut für Sonnensystemforschung, Justus-von-Liebig-Weg 3, D-37077 Göttingen, Germany*
[10] *Institut de Recherche en Astrophysique et Planétologie, CNRS, Université Paul Sabatier, Observatoire Midi-Pyrénées, 9 Avenue du Colonel Roche, F-31028 Toulouse Cedex 4, France*

Accepted 2019 July 24. Received 2019 July 16; in original form 2019 April 12

ABSTRACT

Comets are considered to be some of the most pristine and unprocessed Solar system objects accessible to *in situ* exploration. Investigating their molecular and elemental composition takes us on a journey back to the early period of our Solar system and possibly even further. In this work, we deduce the bulk abundances of the major volatile species in comet 67P/Churyumov-Gerasimenko, the target of the European Space Agency's (ESA) *Rosetta* mission. The basis are measurements obtained with the ROSINA instrument suite on board the *Rosetta* orbiter during a suitable period of high outgassing near perihelion. The results are combined with both gas and dust composition measurements published in the literature. This provides an integrated inventory of the major elements present in the nucleus of 67P/Churyumov-Gerasimenko. Similar to comet 1P/Halley, which was visited by ESA's *Giotto* spacecraft in 1986, comet 67P/Churyumov-Gerasimenko also shows near-solar abundances of oxygen and carbon, whereas hydrogen and nitrogen are depleted compared to solar. Still, the degree of devolatilization is lower than that of inner Solar system objects, including meteorites and the Earth. This supports the idea that comets are amongst the most pristine objects in our Solar system.

Key words: comets: general – comets: individual: 67P/Churyumov-Gerasimenko.

1 INTRODUCTION

Comets were formed by the accretion of condensed matter originating from various nucleosynthetic processes (Geiss 1987). As such, they contain sizeable amounts of volatile species in the form of ices next to lesser volatile organics all the way to refractory material. The origin of the material is still debated. The relative abundances of volatile materials, in particular, indicate an interstellar medium (ISM) origin

---

★ E-mail: martin.rubin@space.unibe.ch

(Bockelée-Morvan et al. 2000), where chemistry in the icy mantles of grains played an important role (Herbst & van Dishoeck 2009). Cold temperatures in the ISM also affect isotopic ratios, in particular the deuteration of molecules (Furuya, van Dishoeck & Aikawa 2016), and hence several isotopic ratios in the volatile species also point to an origin in the ISM (Bockelée-Morvan et al. 2015).

On the other hand, a large number of high temperature condensates that were processed close to the Sun or by shocks in the disc have been identified in the samples returned by NASA's Stardust mission to comet Wild 2 (Brownlee et al. 2006; McKeegan et al. 2006). Therefore, looking at comets as a whole, multiple processes must have been at work in forming the material they are made from and distributing it in the Solar system. Molecular and elemental abundances thus contain crucial clues to the origin of the cometary material and the subsequent processing during or even before the formation of the Solar system.

Addressing these questions was one of the main goals of the European Space Agency's (ESA) *Rosetta* mission to the Jupiter Family Comet (JFC) 67P/Churyumov-Gerasimenko (Schwehm & Schulz 1999; Glassmeier et al. 2007). *Rosetta* followed the comet for more than 2 yr starting in 2014 August to the end of 2016 September. The spacecraft carried a suite of instruments dedicated to a close investigation, including the lander Philae that was successfully deployed on the surface of the nucleus in November 2014 (Bibring et al. 2015).

Compositional measurements of comet 67P/Churyumov-Gerasimenko (hereafter 67P/C-G) were carried out with several instruments. Volatile species were measured by Alice (Feldman et al. 2015), VIRTIS (Visible and Thermal Infrared Thermal Imaging Spectrometer; Bockelée-Morvan et al. 2016), ROSINA (*Rosetta* Orbiter Spectrometer for Ion and Neutral Analysis; Le Roy et al. 2015), and OSIRIS (Optical, Spectroscopic, and Infrared Remote Imaging System; Bodewits et al. 2016) on board the *Rosetta* spacecraft and by Ptolemy (Wright et al. 2015) and COSAC (Cometary Sampling and Composition; Goesmann et al. 2015) on board the lander Philae.

ROSINA was the mass spectrometer suite on board *Rosetta* dedicated to the *in situ* measurement of the volatile material emanating from the comet's nucleus (Balsiger et al. 2007). ROSINA consisted of the Double Focusing Mass Spectrometer (DFMS), the Reflectron-type Time-Of-Flight mass spectrometer (RTOF), and the Comet Pressure Sensor (COPS). The two mass spectrometers complemented each other with high time-resolution, mass-resolution, sensitivity, and dynamic range.

ROSINA observations revealed a plethora of volatiles released from the nucleus already at a heliocentric distance beyond 3 au (Le Roy et al. 2015). The most abundant volatiles, H_2O, CO_2, and CO, were shown to exhibit a pronounced heterogeneous distribution in the coma (Hässig et al. 2015; Hoang et al. 2017). Highly volatile O_2, found in similar quantity as CO_2 and CO, showed a good correlation to H_2O (Bieler et al. 2015; Gasc et al. 2017a). Numerical models of the most abundant volatiles of the comet were then used to quantify the activity and its distribution on the surface (Fougere et al. 2016b; Hansen et al. 2016; Marschall et al. 2017; Zakharov et al. 2018; Läuter et al. 2019). In addition, species with (much) lower abundances including a host of S-bearing molecules (Calmonte et al. 2016), hydrocarbons and oxygenated compounds (Schuhmann et al. 2019a,b), noble gases (Balsiger et al. 2015; Marty et al. 2017; Rubin et al. 2018), hydrogen halides (Dhooghe et al. 2017), and N_2 (Rubin et al. 2015a) were detected during various phases of the mission.

The abundances in the refractory elements in the dust of 67P/C-G were further measured by the Comet Secondary Ion Mass Spectrometer (COSIMA; Kissel et al. 2007) and presented by Bardyn et al. (2017). Grains collected on COSIMA's exposed target were bombarded with an 8 keV indium ion beam and the ions sputtered off the dust were detected by a micro-channel plate (MCP) detector after mass-separation in a time-of-flight section. Given the collector temperature of around 283 K, COSIMA was most sensitive to the refractory material and the less volatile organics (Fray et al. 2016) that remained on the collectors for up to several days or even weeks without evaporating.

In this paper, we report on the deduced bulk abundances of the volatile species in comet 67P/C-G. For this purpose, we used ROSINA data to derive relative abundances of CO_2, CO, O_2, NH_3, HCN, HCNO, CH_3NO, CH_3CN, HC_3N and their isomers with respect to H_2O for a suitable period near perihelion. These results were then combined with relative abundances derived from ROSINA data in the same fashion from published literature. The following section presents the two ROSINA instruments used in this work, DFMS and COPS, and the analytical technique used to derive relative abundances from the measurements. The next section discusses the measurement period selected for deducing the bulk abundances of the volatile material in the comet's nucleus. Afterwards, we present a collection of our results together with previously published bulk abundances derived from ROSINA observations. The elemental abundances in 67P/C-G's ices follow from these data, and when combined with COSIMA results, the elemental ratios in 67P/C-G's nucleus as well. The last section discusses our findings and compares them with other objects in our Solar system.

2 INSTRUMENT DESCRIPTION AND DATA REDUCTION

DFMS was a high-resolution, high-sensitivity mass spectrometer built in double-focusing configuration (Mattauch & Herzog 1934). Neutral gas particles from the comet entered DFMS' ion source, where they were ionized and partially fragmented by 45 eV electrons emitted by a hot filament. After ionization, the ions were accelerated and deflected by 90° in the electric field of the curved electrostatic analyser. After another deflection by 60° in a permanent magnet, they passed the zoom optics, where the ion beam was widened before it impacted the MCP detector. The resulting mass resolution was $m/\Delta m = 3000$ for a mass/charge ratio of 28 u/e at 1 per cent of the peak height (Balsiger et al. 2007). For mass/charge ratios of $m/Q \geq 70$ u/e, an additional post-acceleration potential was applied in front of the detector to increase the detection efficiency for the heavier species. The avalanche of electrons produced by each impact on the MCP was collected on the position-sensitive Linear Electron Detector Array's (LEDA) two parallel rows of 512 pixels each, which were operated in analogue mode (Nevejans et al. 2002).

Each mass-to-charge ratio was measured separately in a sequential order. A suitable set of potentials would first be applied for a given mass-to-charge ratio and the voltage across the MCP adjusted to guarantee suitable amplification while avoiding saturation. This allowed variation of the gain between each measurement, resulting in a high dynamic range of the order of 10^{10}. Setting the voltages took roughly

10 s per spectrum. Each mass would then be accorded 20 s of integration time before moving on to the next mass. Hence, a full scan in the typical mass range from 13 u/e to 100 u/e lasted approximately 45 min. This includes the two additional 18 u/e measurements performed at the beginning and end of each measurement mode to monitor changes in the activity of the comet.

DFMS was used to derive relative abundances of the individual species with respect to water. To do so, linear time-interpolations between adjacent measurements of the same species were performed and related to water, which was used as reference. In the aforementioned measurement technique, ions impacted the MCP with different velocities and energies. All Level-3 data available through ESA's Planetary Science Archive (PSA) thus contains corrections for the MCP detector's yield (relative to neon) as derived during calibrations. With a_X: the number of counts for a given species X interpolated to a given time, S_X: its calibrated sensitivity, Y_X: its yield, $W_X = S_X Y_X$: its yield-corrected sensitivity, and $f_{X\rightarrow X^+}$: the fragmentation branching of neutral species X to its parent ion X^+, the relative abundance of e.g. carbon dioxide with respect to water can be computed with

$$r_{CO_2} = \frac{n_{CO_2}}{n_{H_2O}} = \frac{a_{CO_2}\ \cos\left(\vartheta_{H_2O}\right)\ W_{H_2O}\ f_{H_2O\rightarrow H_2O^+}}{a_{H_2O}\ \cos\left(\vartheta_{CO_2}\right)\ W_{CO_2}\ f_{CO_2\rightarrow CO_2^+}}\,, \tag{1}$$

where ϑ_X corresponds to the off-nadir pointing angle during the time of the measurement of species X. Thus, $\cos(\vartheta_X)$ represents the geometrical cross-section of DFMS' ion source that is exposed to the comet. Data obtained at times when the spacecraft was pointing more than 30° off from the nadir direction have been excluded from the dataset. Additionally, considering that all species were measured within $\sim$20 min of a water measurement and slew rates were slow, the $\cos(\vartheta_{H_2O})/\cos(\vartheta_X)$-correction tends to be small.

The case of e.g. carbon monoxide is more complicated compared to the example above as the fragmentation of CO_2 and H_2CO to CO^+ inside the ion source has to be taken into account by subtracting the corresponding signal from the fragmentation $f_{X\rightarrow Y^+}$ of neutral species X to its fragment ion Y^+ as follows:

$$r_{CO} = \frac{n_{CO}}{n_{H_2O}} = \frac{\left(\frac{a_{CO}}{Y_{CO}} - \frac{a_{CO_2}}{Y_{CO_2}}\frac{f_{CO_2\rightarrow CO^+}}{f_{CO_2\rightarrow CO_2^+}} - \frac{a_{H_2CO}}{Y_{H_2CO}}\frac{f_{H_2CO\rightarrow CO^+}}{f_{H_2CO\rightarrow H_2CO^+}}\right) W_{H_2O}\ Y_{CO}\ f_{H_2O\rightarrow H_2O^+}}{a_{H_2O}\ W_{CO}\ f_{CO\rightarrow CO^+}}. \tag{2}$$

For the sake of readability, we have omitted the off-nadir correction from this equation. Additional contributions to the CO^+ signal from fragmentations of larger molecules were treated similarly. The same approach was taken with other species similarly affected by contributions from higher mass molecules, such as formaldehyde and methanol's contribution to it ($CH_3OH + e^- \rightarrow H_2CO^+ + 2H + 2e^-$). Gasc et al. (2017b) presented a simplified version of these equations for the analysis of RTOF data, given that the different species are measured contemporaneously in a time-of-flight instrument.

The relative abundances r_X of the volatile species $X = \{H_2O,\ CO,\ CO_2,\ O_2,\ H_2CO,\ \ldots\}$ can now be derived with respect to water. Details on the ROSINA calibrated sensitivities S_X and fragmentation patterns $f_{X\rightarrow Y^+}$ can be obtained from PSA, along with the Level-3 ROSINA datasets. For species that were not calibrated due to their toxicity or corrosiveness, we have applied the empirical formula for the sensitivity derived by Calmonte (2015) and included fragmentation patterns obtained from reference spectra published by the National Institute of Standards and Technology (NIST; Kim et al. 2005). Sensitivity errors for the individual species are of the order of 15–20 per cent. An additional error of 20 per cent is applicable for the uncertainty of the detector's gain calibration as well as aging processes caused by the accumulated lifetime charge, which differs from one pixel to the next (cf. Schroeder et al. 2018). Furthermore, counting statistics and, in the case of overlapping peaks, a fitting error have been included (cf. Marty et al. 2017; Rubin et al. 2018). The DFMS calibration factors used in this work have been summarized in Table 1.

The COPS sensor contained two gauges, the Nude Gauge (NG) and the Ram Gauge. Here, we used the NG, an open source where 150 eV electrons ionized the ambient neutral gas passing through the gauge. The ions formed inside the open volume were then accelerated towards a cathode, and the ion current was measured after a suitable amplification. The ion current relative to the electron current is related to the density of the neutral gas inside the NG after application of the laboratory-derived calibration factors (Graf et al. 2004; Tzou 2017). The simplicity of the sensor makes it a reliable and stable monitor for the gas density of the comet in the vicinity of the spacecraft. No measurable change in calibration parameters has been observed for the laboratory twin of COPS throughout its operation time (Tzou 2017) despite heavy use.

COPS itself could not derive the composition of the gas. Therefore, COPS was calibrated for a 100 per cent N_2 reference atmosphere (cf. Gasc et al. 2017b). For other compositions, a set of correction factors has to be applied, as each species has its own ionization cross-section and hence a different sensitivity. The measured density is thus an N_2-equivalent and corresponds to the sum of the corrected partial densities

$$n_{COPS} = n_{N_2} = \sum_X \frac{n_X}{\beta_X} = n_{H_2O} \sum_X \frac{n_X}{n_{H_2O}\beta_X}, \tag{3}$$

where β_X is the correction factor for species X with respect to N_2. This factor can be obtained from calibration or from the ratio of the total ionization cross-section of species X with respect to N_2 for 150 eV electrons. The COPS correction factors used in this work can be found in Table 1. The density of water molecules can then be computed by using the relative abundance of species X with respect to water, r_X, derived from DFMS

$$n_{H_2O} = \frac{n_{COPS}}{\sum_X \frac{n_X}{n_{H_2O}\beta_X}} = \frac{n_{COPS}}{\sum_X \frac{r_X}{\beta_X}}\,. \tag{4}$$

Table 1. Calibration factors used for a subset of the volatile species detected at 67P/C-G, including the ones presented in this work.

Species	Sensitivity (cm^3) $W_X = S_X\, Y_X$	Yield correction relative to neon Y_X	COPS correction w.r.t. N$_2$ β_X	Fragmentation (w.r.t. total ionization cross section) $f_{X\rightarrow Y^+}$	
H_2O	2.04×10^{-19}	0.886	0.893	$H_2O \rightarrow H_2O^+$	0.792
CO_2	3.29×10^{-19}	2.141	0.704	$CO_2 \rightarrow CO_2{}^+$	0.779
				$CO_2 \rightarrow CO^+$	0.099
CO	2.88×10^{-19}	1.420	0.952	$CO \rightarrow CO^+$	0.964
O_2	2.57×10^{-19}	1.623	0.990	$O_2 \rightarrow O_2{}^+$	0.821
CH_4	6.85×10^{-19}	0.790	0.654	$CH_4 \rightarrow CH_4{}^+$	0.522
C_2H_6	3.50×10^{-19}	1.526	0.380	$C_2H_6 \rightarrow C_2H_6{}^+$	0.106
C_3H_8	8.91×10^{-19}	2.144	0.262	$C_3H_8 \rightarrow C_3H_8{}^+$	0.098
C_6H_6	4.66×10^{-18}	2.624	0.172	$C_6H_6 \rightarrow C_6H_6{}^+$	0.387
CH_3OH	1.12×10^{-18}	1.624	0.541	$CH_3OH \rightarrow H_2CO^+$	0.030
				$CH_3OH \rightarrow CH_3OH^+$	0.130
C_2H_5OH	6.99×10^{-19}	2.232	0.335	$C_2H_5OH \rightarrow H_2CO^+$	0.0083
				$C_2H_5OH \rightarrow CH_3CHO^+$	0.0083
				$C_2H_5OH \rightarrow C_2H_5OH^+$	0.030
H_2CO	4.86×10^{-19}	1.525	0.631	$H_2CO \rightarrow H_2CO^+$	0.309
CH_3CHO	6.90×10^{-19}	2.143	0.385	$CH_3CHO \rightarrow H_2CO^+$	0.0044
				$CH_3CHO \rightarrow CH_3CHO^+$	0.146
HCOOH	4.72×10^{-19}	2.230	0.478	$HCOOH \rightarrow H_2CO^+$	0.0063
				$HCOOH \rightarrow HCOOH^+$	0.227
CH_3COOH	6.16×10^{-19}	3.047	0.309	$HCOOCH_3 \rightarrow H_2CO^+$	0.0012
				$HCOOCH_3 \rightarrow CH_3CHO^+$	0.0074
				$HCOOCH_3 \rightarrow HCOOCH_3{}^+$	0.222
NH_3	3.83×10^{-19}	0.837	0.787	$NH_3 \rightarrow NH_3{}^+$	0.475
HCN	4.27×10^{-19}	1.367	0.645	$HCN \rightarrow CN^+$	0.133
				$HCN \rightarrow HCN^+$	0.792
HNCO	3.51×10^{-19}	2.099	0.669	$HNCO \rightarrow CN^+$	0.013
				$HNCO \rightarrow HCN^+$	0.012
				$HNCO \rightarrow CO^+$	0.030
				$HNCO \rightarrow HNCO^+$	0.674
CH_3NO	5.67×10^{-19}	2.186	0.402	$CH_3NO \rightarrow CN^+$	0.0053
				$CH_3NO \rightarrow HCN^+$	0.031
				$CH_3NO \rightarrow HNCO^+$	0.045
				$CH_3NO \rightarrow CH_3NO^+$	0.411
CH_3CN	6.27×10^{-19}	2.017	0.386	$CH_3CN \rightarrow CH_3CN^+$	0.511
HC_3N	6.02×10^{-19}	2.483	0.349	$HC_3N \rightarrow HC_3N^+$	0.593
H_2S	1.21×10^{-19}	1.717	0.455	$H_2S \rightarrow H_2S^+$	0.574
OCS	3.94×10^{-19}	3.044	0.532	$OCS \rightarrow OCS^+$	0.528
SO_2	3.68×10^{-19}	3.240	0.455	$SO_2 \rightarrow SO_2{}^+$	0.575
CS_2	2.68×10^{-18}	2.590	0.207	$CS_2 \rightarrow CS_2{}^+$	0.664

The abundances of the other volatile species then follow directly from

$$n_X = r_X\, n_{H_2O}. \tag{5}$$

This technique provides a reliable way to derive accurate particle densities and relative abundances and was used throughout the ROSINA data analysis (cf. Gasc et al. 2017b). It is independent of the aging processes of DFMS' MCP detector, provided that all species are, to the first order, affected in the same way by the decreasing MCP amplification over the course of the mission.

3 MEASUREMENTS

ROSINA DFMS measured the relative abundances of many volatile species at the location of the *Rosetta* spacecraft. Besides water, the major volatile species were carbon dioxide (CO_2), carbon monoxide (CO), molecular oxygen (O_2), followed by methane (CH_4), ethane (C_2H_6), formaldehyde (H_2CO), and methanol (CH_3OH).

The ratios varied over the course of the mission and thus did not always reflect their abundance in the bulk ice of the nucleus. Fig. 1 shows the ratios of HCN, HNCO, and CH_3NO (including their isomers) with respect to H_2O that are reported in this work. The measured ratios depend in a non-trivial way on the heliocentric distance, the orientation of 67P/C-G's spin axis, and *Rosetta*'s location with respect to the nucleus (Fougere et al. 2016a; Hansen et al. 2016; Gasc et al. 2017a).

We thus selected the same measurement period from the inbound portion of the comet's orbit as Calmonte et al. (2016), namely 2015 May, to derive the bulk abundances of CO_2, CO, O_2, NH_3, HCN, HCNO, CH_3NO, CH_3CN, HC_3N and their isomers with respect to H_2O in 67P/C-G. Calmonte et al. (2016) proposed this time period to be suitable to deduce bulk abundances of volatile species in the cometary ices.

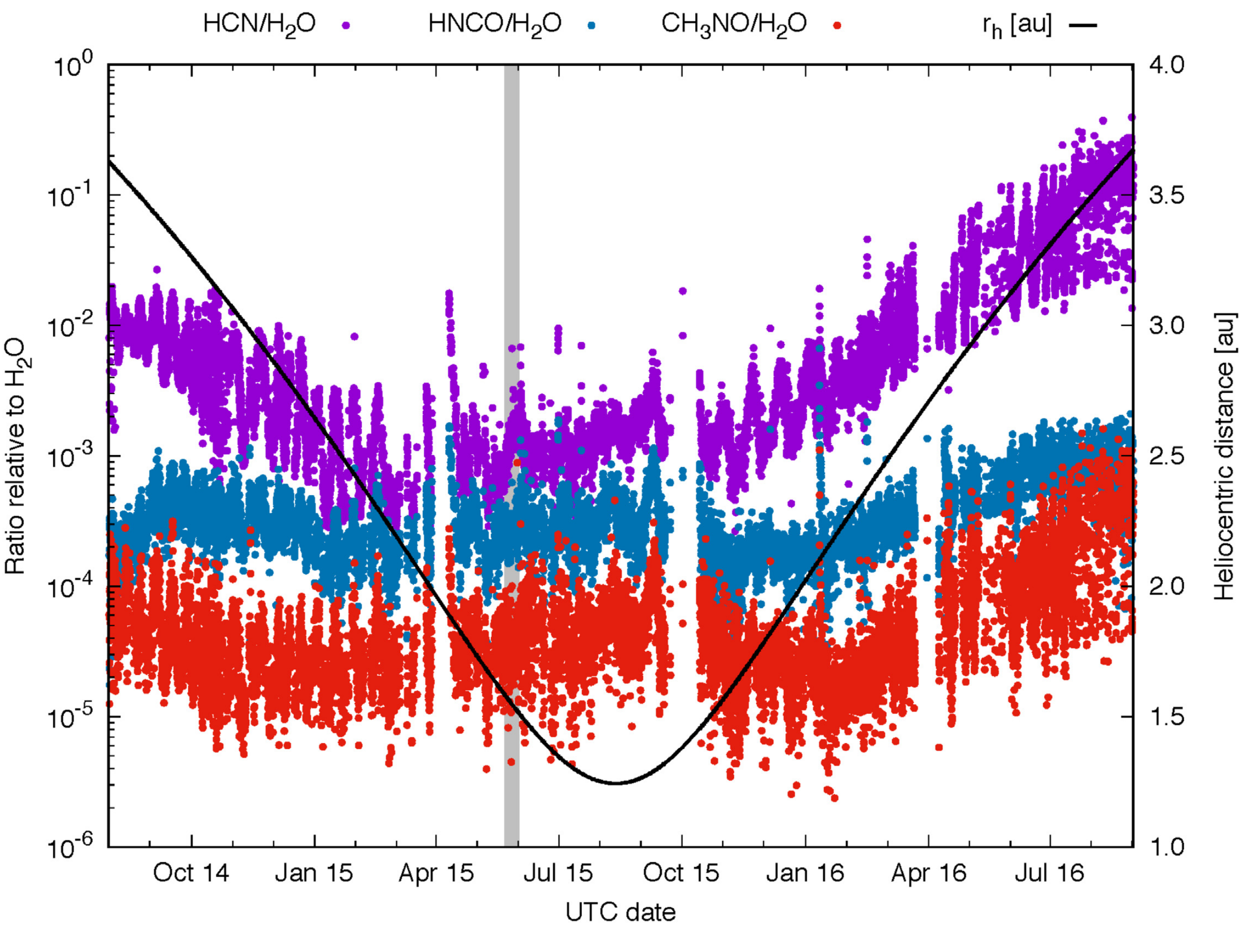

Figure 1. Relative abundances of HCN, HNCO, and CH_3NO (and their isomers) with respect to H_2O and the heliocentric distance (solid black line) throughout most of the mission, including the investigated period indicated in grey (cf. Fig. 2).

The reasons are (a) the high outgassing as the comet approaches perihelion and hence high erosion associated with providing fresh material from the comet's interior, (b) little contamination from outbursts driven by highly volatile species that occurred close to perihelion in 2015 August, and (c) the favourable orbit for an *in situ* instrument such as ROSINA as *Rosetta* passed over the dayside of the nucleus and above the more active Southern summer hemisphere. We hence regard the ratios measured in the coma during this period as representative of the bulk abundances in the ices of 67P/C-G. Fig. 2 shows the details of *Rosetta*'s location with respect to the nucleus. The grey bar at the bottom denotes the selected investigation period, when *Rosetta* was passing over the dayside (phase angles $< 85°$) of the active Southern summer hemisphere (sub-spacecraft latitudes $< 0°$). The same period is also indicated in Fig. 1 for comparison.

The measured relative abundances with respect to water for the period investigated are shown in Fig. 3. The horizontal lines represent the averaged ratios as indicated in the labels together with their corresponding 1σ errors.

The same period in 2015 May has been analysed in previous works on the sulphur-bearing species (Calmonte et al. 2016), hydrocarbons and oxygenated compounds (Schuhmann et al. 2019a,b), halogens (Dhooghe et al. 2017), noble gases, and N_2 (Rubin et al. 2018). We therefore refer to these works for the details and just include the corresponding relative bulk abundances in Table 2.

These results can be compared to measurements obtained earlier in the mission beyond 3.1 au. Le Roy et al. (2015) reported strong differences in the relative abundances with respect to water above the summer and winter hemispheres (reproduced in Table 2). The complex shape of the nucleus combined with the obliquity of the comet's rotation axis (Sierks et al. 2015) of 52° led to a pronounced seasonal outgassing pattern (Hässig et al. 2015). The deduced bulk abundances in Table 2 for the southern summer in 2015 May are within a factor of a few of those measured above the Northern summer hemisphere before equinox (Le Roy et al. 2015). The Northern hemisphere may either be enhanced in water or depleted in CO_2 (and other species of higher volatility). The 2015 May measurements, on the other hand, were obtained much closer to the Sun and hence at a higher relative water activity (cf. Gasc et al. 2017a). Nevertheless, there are a few notable differences in both data sets, including the sulphur-bearing species SO, SO_2, and S_2, which may be partially associated with semi-volatile species in grains (Altwegg et al. 2016; Calmonte et al. 2016). Such grains are subject to higher sublimation rates due to increased grain temperatures at smaller heliocentric distances (Lien 1990), whereas at increased heliocentric distances their presence may remain hidden. This may also be the case for CH_3NO, HC_3N, and their corresponding isomers. The factor of 10 difference for NH_3, on the other hand, requires a different explanation and shall be addressed elsewhere.

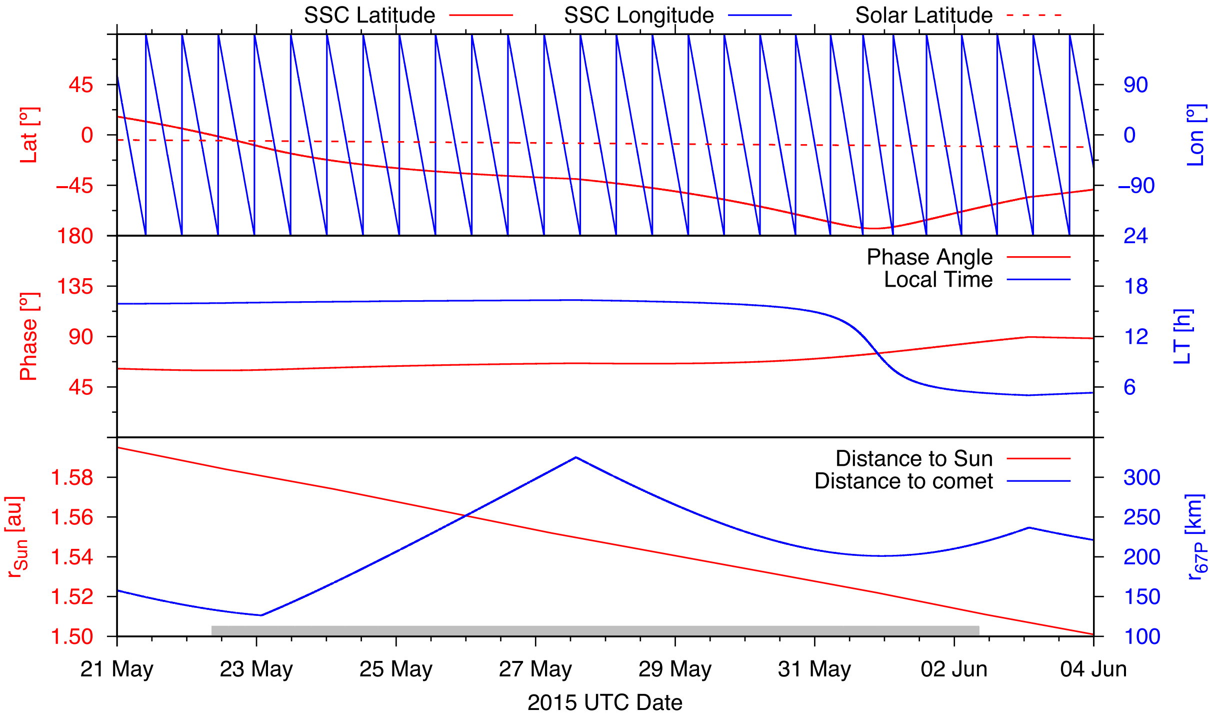

Figure 2. Observation geometry with heliocentric and cometocentric distances in the bottom panel, phase angle and local time in the middle panel, and sub-spacecraft longitude and latitude and sub-solar latitude in the top panel. The investigated period was suitable for deriving bulk abundances in the ices of comet 67P/Churyumov-Gerasimenko (Calmonte et al. 2016) and is indicated by the grey bar at the bottom corresponding to the time when *Rosetta* was above the dayside of the comet (phase angle $< 85°$) and above the more active Southern summer hemisphere (sub-spacecraft latitude $< 0°$).

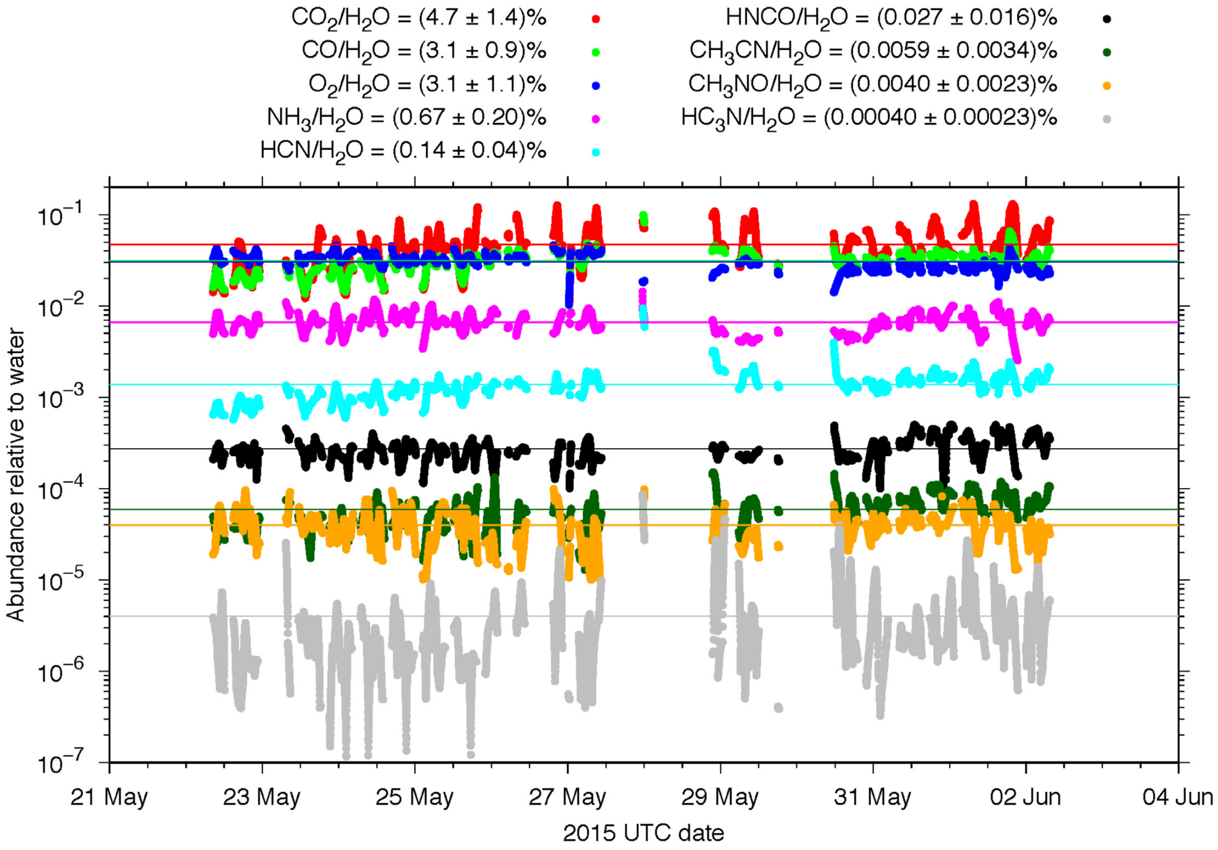

Figure 3. Measured abundances of a suite of volatile species with respect to water from the pre-perihelion period at the end of May 2015, suitable for deriving bulk abundances in the ices of comet 67P/Churyumov-Gerasimenko (Calmonte et al. 2016). The horizontal lines denote the averages for the observed period. Indicated errors represent 1σ.

Table 2. Deduced bulk composition of the ices in comet 67P/Churyumov-Gerasimenko normalized to water based on the 2015 May period. The hydrogen halide abundances have been derived from F/O, Cl/O, and Br/O ratios from Dhooghe et al. (2017) and elemental O-abundances in H_2O, CO_2, CO, and O_2. Calibration values have been used for the indicated component. Additional possible isomers are listed in brackets, as a unique identification is not possible with DFMS. Examples include HCN versus HNC and CH_3CH_2SH versus CH_3SCH_3. Phosphorus has been identified in the form of PO. However, contributions in other forms are possible (see the text). The indicated errors represent 1σ, except for the hydrogen halides where observed ranges were reported. Also given are the abundances measured above the Northern and Southern hemispheres at 3.1 au inbound from Le Roy et al. (2015).

Molecule	Deduced bulk abundance	Northern versus Southern hemispheres at 3.1 au $^{(a)}$	Name (including some isomers)	Reference and notes
H_2O	100	100/100	Water	Definition
CO_2	4.7 ± 1.4	2.5/80	Carbon dioxide	$^{(e)}$, cf. Fig. 3
CO	3.1 ± 0.9	2.7/20	Carbon monoxide	$^{(e)}$, cf. Fig. 3
O_2	3.1 ± 1.1	3.80 ± 0.85 $^{(b)}$	Molecular oxygen	$^{(e)}$, cf. Fig. 3
CH_4	0.34 ± 0.07	0.13/0.56	Methane	$^{(f)}$
C_2H_6	0.29 ± 0.06	0.32/3.3	Ethane	$^{(f)}$
C_3H_8	0.018 ± 0.004		Propane	$^{(f)}$
C_6H_6	0.00069 ± 0.00014		Benzene	$^{(f)}$
C_7H_8	0.0062 ± 0.0012		Toluene	$^{(f)}$
CH_3OH	0.21 ± 0.06	0.31/0.55	Methanol	$^{(g)}$
C_2H_5OH	0.039 ± 0.023		Ethanol (dimethyl ether)	$^{(g)}$
CH_3CH_2CHO	0.0047 ± 0.0024		Propanal (acetone) (propylene oxide)	$^{(g)}$
H_2CO	0.32 ± 0.10	0.33/0.53	Formaldehyde	$^{(g)}$
CH_3CHO	0.047 ± 0.017	0.01/0.024	Acetaldehyde (ethylene oxide) (vinyl alcohol)	$^{(g)}$
HCOOH	0.013 ± 0.008	0.008/0.03	Formic acid	$^{(g)}$
CH_3COOH	0.0034 ± 0.0020	0.004/0.023	Acetic acid (methyl formate) (glycolaldehyde)	$^{(g)}$
$(CH_2OH)_2$	0.011 ± 0.007	$0.0008/ < 0.0025$	Ethylene glycol (methoxymethanol)	$^{(g)}$
$CH_3(CH_2)_2CHO$	0.010 ± 0.003		Butanal (ethoxyethene)	$^{(g)}$
CH_3COOCH_3	0.0021 ± 0.0007		Methyl acetate (propanoic acid) (acetol)	$^{(g)}$
NH_3	0.67 ± 0.20	0.06/0.15	Ammonia	$^{(e)}$, cf. Fig. 3
N_2	0.089 ± 0.024	0.015 to 0.114 $^{(a), (c)}$	Molecular nitrogen	$^{(h)}$
HCN	0.14 ± 0.04	0.09/0.62	Hydrogen cyanide (hydrogen isocyanide)	$^{(e)}$, cf. Fig. 3
HNCO	0.027 ± 0.016	0.016/0.031	Isocyanic acid (cyanic acid)	$^{(e)}$, cf. Fig. 3
CH_3NO	0.0040 ± 0.0023	$<0.0001/0.001$	Formamide (formaldoxime) (oxaziridine)	$^{(e)}$, cf. Fig. 3
CH_3CN	0.0059 ± 0.0034	0.006/0.016	Acetonitrile (isocyanomethane)	$^{(e)}$, cf. Fig. 3
HC_3N	0.00040 ± 0.00023	$< 0.00002/ < 0.0005$	Cyanoacetylene (isocyanoacetylene)	$^{(e)}$, cf. Fig. 3
H_2S	1.10 ± 0.46	0.67/1.75	Hydrogen sulphide	$^{(i)}$
OCS	$0.041^{+0.082}_{-0.020}$	0.017/0.098	Carbonyl sulphide	$^{(i)}$
SO	$0.071^{+0.142}_{-0.037}$	0.004/0.0014	Sulfur monoxide	$^{(i)}$
SO_2	$0.127^{+0.254}_{-0.064}$	0.011/0.041	Sulfur dioxide	$^{(i)}$
CS_2	$0.0057^{+0.0114}_{-0.0028}$	0.003/0.024	Carbonyl sulphide	$^{(i)}$
S_2	$0.0020^{+0.0040}_{-0.0010}$	0.0004/0.0013	Sulfur dimer	$^{(i)}$
H_2CS	$0.0027^{+0.0058}_{-0.0024}$		Thioformaldehyde	$^{(i)}$
S	0.46 ± 0.36		Atomic sulphur	$^{(i)}$
CH_3SH	$0.038^{+0.079}_{-0.028}$		Methanethiol	$^{(i)}$
CH_3CH_2SH CH_3SCH_3	$0.00058^{+0.00123}_{-0.00049}$		Ethanethiol Dimethyl sulphide	$^{(i)}$

Table 2 – *continued*

Molecule	Deduced bulk abundance	Northern versus Southern hemispheres at 3.1 au [(a)]	Name (including some isomers)	Reference and notes
Ar	0.00058 ± 0.00022	0.00012 to 0.0027 [(d)]	Argon	[(h)]
Kr	0.000049 ± 0.000022		Krypton	[(h)]
Xe	0.000024 ± 0.000011		Xenon	[(h)]
Ne	<0.000005		Neon	[(h)], upper limit
HF	$0.011^{+0.037}_{-0.008}$		Hydrogen fluoride	[(j)], range given
HCl	$0.014^{+0.045}_{-0.012}$		Hydrogen chloride	[(j)], range given
HBr	$0.00030^{+0.00053}_{-0.00018}$		Hydrogen bromide	[(j)], range given
PO	$0.011^{+0.022}_{-0.006}$		Phosphorous oxide	[(k)]

Note. References: (a) Le Roy et al. (2015), (b) Bieler et al. (2015), (c) Rubin et al. (2015a), (d) Balsiger et al. (2015), (e) this work, (f) Schuhmann et al. (2019a), (g) Schuhmann et al. (2019b), (h) Rubin et al. (2018), (i) Calmonte et al. (2016), (j) Dhooghe et al. (2017), (k) Rivilla et al. (in preparation).

DFMS measured density ratios *in situ* at the location of *Rosetta*; however, deriving nucleus outgassing flux ratios depends also on the velocities of the individual species. Analogous to Rubin et al. (2018), we have assumed collisional coupling of the gases in the near nucleus environment at small heliocentric distances, which in effect equilibrates the different outflow velocities. This is supported by numerical simulations (Tenishev, Combi & Davidsson 2008). As a result, the measured density ratios at the spacecraft can be converted directly into the ratio of the outgassing fluxes from the cometary surface.

Some of the volatile species reported here have also been observed by other scientific instruments on board Rosetta, including CO_2, CH_4, and OCS by VIRTIS (Bockelée-Morvan et al. 2016) and H_2O by MIRO (Marshall et al. 2017). In particular, MIRO measurements (Biver et al. 2019) indicate a lower amount of water near perihelion compared to ROSINA-derived water production rates (Hansen et al. 2016). Consequentially, their relative abundances with respect to water may be different. This is in part due to the time period selected for analysis, though several other possible explanations have also been put forward. For instance, distributed sources of volatile species near the nucleus, where a portion of the volatile species are trapped in grains, would be invisible to remote sensing instruments. While some of the volatile species have indeed been shown to be associated with grains (Altwegg et al. 2016; De Keyser et al. 2017), no clear indication for distributed sources was found for water, and Biver et al. (2019) estimated an upper limit of 50 per cent for contributions from grains. For our analysis, we assumed that grains moving at $\sim 1\ \mathrm{m\ s^{-1}}$ would have lost their volatiles by the time they reached *Rosetta* (Lien 1990), which was more than 100 km from the nucleus. This is in line with numerical models of the major volatile species H_2O, CO_2, CO, and O_2 (Fougere et al. 2016b; Läuter et al. 2019), reproducing ROSINA data within error bars without the use of any distributed sources.

An alternative approach to estimate the relative bulk abundances of the volatile material in a comet is to integrate the total production of volatile species over the entire apparition and relate it to the total water production. This approach is model-dependent and may not be possible for minor species, which were below DFMS' detection limit for large parts of the mission. Nevertheless, this approach has been carried out by Läuter et al. (2019) for the major molecules H_2O, CO_2, CO, and O_2 by inverting an analytically described outgassing pattern of thousands of surface elements and optimizing their activity to fit the tens of thousands of ROSINA measurements. Over the 2 yr when *Rosetta* was accompanying the comet, the relative losses were $r_{CO_2} = (5.9 \pm 3.0) \times 10^{-2}$, $r_{CO} = (2.3 \pm 1.0) \times 10^{-2}$, and $r_{O_2} = (1.6 \pm 0.7) \times 10^{-2}$. The corresponding numbers by Combi et al. (in preparation) are $r_{CO_2} = 7.4 \times 10^{-2}$, $r_{CO} = 2.7 \times 10^{-2}$, and $r_{O_2} = 1.6 \times 10^{-2}$ and are based on a fully kinetic Direct Simulation Monte Carlo model that represents the molecules and their interaction in the coma by a much smaller set of weighted model particles. These relative numbers may also be seen as an estimate for the bulk abundance of the volatiles in 67P/C-G, assuming that outgassing during the remaining part of 67P/C-G's orbit through its aphelion can be neglected.

Some of the deviations of our results based on the May 2015 period in Table 2 compared to the integrals over the whole mission from Läuter et al. (2019) and Combi et al. (in preparation) can be explained by the different methods used. Late in the mission, at heliocentric distances beyond ~3 au, CO_2 became the dominant species as H_2O outgassing decreased sharply (Hansen et al. 2016; Läuter et al. 2019). Consequentially, the integral over the entire mission yields a CO_2/H_2O ratio that is about 25 per cent higher. Nevertheless, the ratios obtained by Läuter et al. (2019) have overlapping error bars with those for the ratios derived for the end of 2015 May period. The three approaches yield a somewhat lower O_2/H_2O compared to $r_{O_2} = (3.80 \pm 0.85) \cdot 10^{-2}$ by Bieler et al. (2015). This difference is a consequence of a decreasing amount of O_2 with respect to H_2O towards perihelion (Bieler et al. 2015; Fougere et al. 2016b; Läuter et al. 2019; Combi et al. in preparation).

Table 2 lists a collection of derived bulk abundances in the ices of comet 67P/Churyumov-Gerasimenko, including earlier works on sulphur (Calmonte et al. 2016), halogens (Dhooghe et al. 2017), noble gases, and N_2 (Rubin et al. 2018). Furthermore, Rivilla et al. (in preparation) identified phosphorous monoxide, PO, as the main carrier of phosphorus in the comet. Table 2 also lists the deduced abundance of PO, assuming its correlation to SO, derived at a heliocentric distance of 3 au, also applies to 2015 May. PO_x with $x \geq 2$ has not been identified in DFMS mass spectra. Only upper limits could be established for PH_3 and PN due to interference from $^{18}O^{16}O$ and $CH^{32}S$, respectively. On the other hand, an additional contribution from phosphorus in its elemental form could not be excluded.

Several of the components listed in Table 2 may have been present in the form of a different isomer, possibly even from another chemical functional group. The exact identification of the parent, however, cannot be derived with DFMS, e.g. in the case of hydrogen cyanide versus hydrogen isocyanide (HCN versus HNC; Le Roy et al. 2015) and ethanethiol versus dimethyl sulphide (CH_3CH_2SH versus CH_3SCH_3;

Table 3. Elemental abundances in the ices of comet 67P/Churyumov-Gerasimenko based on Table 2 (left) and in the refractories (right) measured by COSIMA from Bardyn et al. (2017). All ratios are normalized to oxygen.

Element	Ratio volatiles	Ratio refractories
H/O	$1.75^{+0.11}_{-0.10}$	$0.99^{+1.14}_{-0.57}$
O/O	1.0 (definition)	1.0 (definition)
C/O	$8.29^{+2.64}_{-2.53} \times 10^{-2}$	$1.00^{+1.75}_{-0.94}$
S/O	$1.55^{+1.19}_{-0.83} \times 10^{-2}$	–
N/O	$8.51^{+2.66}_{-2.65} \times 10^{-3}$	$3.47^{+7.05}_{-3.47} \times 10^{-2}$
Cl/O	$1.19^{+3.77}_{-0.99} \times 10^{-4}$	–
P/O	$0.92^{+1.84}_{-0.46} \times 10^{-4}$	–
F/O	$0.88^{+3.08}_{-0.69} \times 10^{-4}$	–
Ar/O	$4.84^{+1.86}_{-1.86} \times 10^{-6}$	–
Br/O	$2.48^{+4.46}_{-1.49} \times 10^{-6}$	–
Kr/O	$4.09^{+1.85}_{-1.85} \times 10^{-7}$	–
Xe/O	$2.00^{+0.93}_{-0.92} \times 10^{-7}$	–
Ne/O	$<4.17^{+0.24}_{-0.23} \times 10^{-8}$	–
Si/O	–	$1.84^{+2.89}_{-1.39} \times 10^{-1}$
Fe/O	–	$5.26^{+6.09}_{-3.05} \times 10^{-2}$
Mg/O	–	$2.11^{+3.22}_{-1.61} \times 10^{-2}$
Na/O	–	$1.47^{+3.41}_{-1.27} \times 10^{-2}$
Al/O	–	$3.21^{+6.23}_{-2.69} \times 10^{-3}$
Ca/O	–	$1.00^{+1.40}_{-0.72} \times 10^{-3}$
Mn/O	–	$7.89^{+9.28}_{-4.84} \times 10^{-4}$
Cr/O	–	$4.89^{+6.54}_{-3.38} \times 10^{-4}$
K/O	–	$3.89^{+5.79}_{-2.91} \times 10^{-4}$

Note. H abundance in the refractories (right column) is estimated (Bardyn et al. 2017).

Calmonte et al. 2016). The identification of parent molecules based on the different fragmentation patterns is also very difficult due to the high number of molecules contributing to an even larger suite of daughter species and the presence of a large fraction of unsaturated CH-, CHO-, CHS-, and CHON-bearing species (Altwegg et al. 2017b; Schuhmann et al. 2019a,b). To complicate matters further, a mix of the different isomers may also be present at the same time. As a consequence of this, Table 2 lists which parent was assumed when deriving abundances with the corresponding calibration values from Table 1. However, it is possible that a component is fully or partially present in the form of different isomers and hence some of the possibilities are listed in brackets. Comparing ionization cross-sections and, in particular, fragmentation patterns amongst the different isomers from NIST and laboratory calibrations, differences of up to 50 per cent in the abundances may result from the lack of precise identification of the corresponding molecule(s).

Based on the abundances of volatile species presented in Table 2, the elemental abundances in the volatile species of comet 67P/C-G were derived. A summary is presented in Table 3, where all elements have been normalized to oxygen and sorted by their relative abundance in the volatile phase. The most abundant elements are hydrogen and oxygen as a consequence of water being the dominant volatile species in the comet. The S/O ratio takes all O-bearing molecules from Table 2 into account and thus differs slightly from $S/O = 1.47 \times 10^{-2}$ by Calmonte et al. (2016) based on H_2O, CO_2, CO, and O_2 for the period between the equinox and perihelion. The same also applies to the F/O, Cl/O, and Br/O ratios that were derived in Dhooghe et al. (2017) based on the main O-bearing molecules H_2O, CO_2, CO, and O_2.

As discussed above, the mass range of DFMS does not include mass/charge $m/Q = 2$ u/e, thus the contribution of molecular hydrogen as a cometary parent species has not been accounted for in these calculations. In the case of comet C/2001 A2 (LINEAR), however, Feldman, Weaver & Burgh (2002) showed that the observed H_2 in the coma can be satisfactorily accounted for by photodissociated H_2O.

Bardyn et al. (2017) presented elemental abundances in the refractory phase of comet 67P/C-G. From COSIMA measurements, the presence of high abundances of organic molecules was inferred (Fray et al. 2016), where 45 per cent by weight of the analysed matter share similarities with the Insoluble Organic Matter (IOM) found in carbonaceous chondrites. The resulting ratios, normalized to oxygen, have been reproduced in Table 3 for comparison. A subset of these refractory species was also measured with ROSINA: Wurz et al. (2015) reported elemental abundances of the sputtered refractory species Na, K, and Ca relative to Si. Early in the mission, the solar wind still reached parts of the surface of nucleus, whereas above other areas, increased activity led to collisions in the coma gas and the attenuation of the solar wind (Fuselier et al. 2015; Wurz et al. 2015). Nevertheless, the Na/Si, K/Si, and Ca/Si ratios measured by both COSIMA and ROSINA are in agreement.

Combining the elemental ratios from both the refractory and the volatile phases together with the dust-to-ice ratio (D/I) inside the nucleus provides the elemental ratios in the comet. This shall be discussed in the next section.

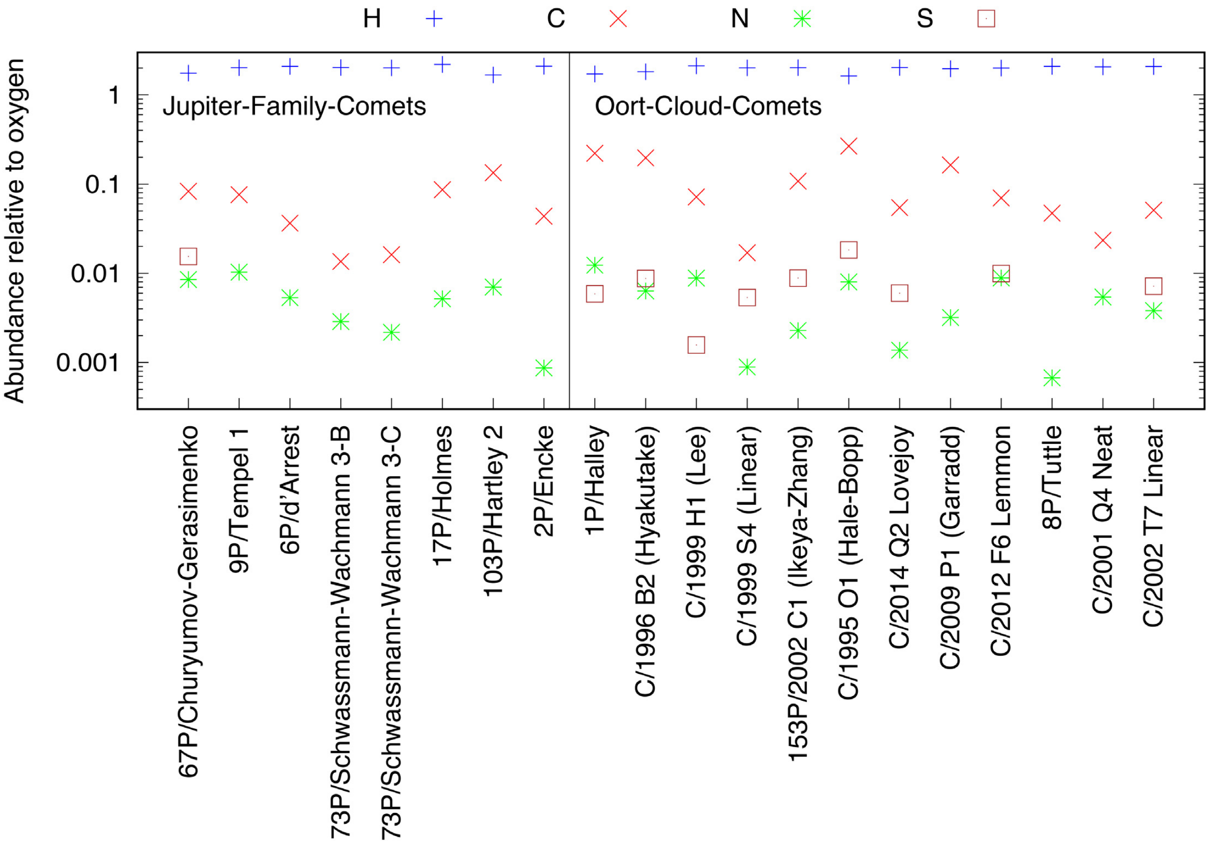

Figure 4. Elemental abundances in the volatile species normalized to oxygen for various comets. Data are taken from Feldman et al. (1987), Eberhardt (1999), and Rubin et al. (2015b) for 1P/Halley; Biver et al. (1999) for Hyakutake; Bockelée-Morvan et al. (2004) and references therein for Lee, Ikeya-Zhang, Hale-Bopp, S4 Linear, and Hyakutake; DiSanti et al. (2006) for T7 Linear; Remijan et al. (2006) and Biver et al. (2007) for Neat and T7 Linear; Böhnhardt et al. (2008), Bonev et al. (2008), and Kobayashi et al. (2010) for Tuttle; Paganini et al. (2012) for Garradd; Fougere et al. (2013) for CO_2 estimate in Hartley 2; Biver et al. (2014) for Hale-Bopp, Lovejoy, and Lemmon; Biver et al. (2016) for Lovejoy and Lemmon; and Dello Russo et al. (2016) with references therein for Hyakutake, Encke, S4 Linear, Ikeya-Zhang, Tempel 1, d'Arrest, Schwassmann-Wachmann 3, Holmes, Hartley 2, and Lee.

4 DISCUSSION AND CONCLUSIONS

The coma of comet 67P/C-G contains a whole suite of low-temperature volatile species. The measured ratios amongst these molecules have been used to derive the structure and the formation temperature of the ices in comet 67P/C-G (Rubin et al. 2015a). From the $N_2/CO = (5.70 \pm 0.66)$‰ measured early in the mission at ∼3.1 au, Rubin et al. (2015a) derived a formation temperature between 24 and 27 K based on laboratory measurements of the relative trapping efficiencies of N_2 versus CO in amorphous water ice at different temperatures (Bar-Nun, Notesco & Owen 2007). The case of a crystalline origin of the cometary ices, i.e. the reconfiguration of the ices in the protosolar nebula, was studied by Lectez et al. (2015) and yielded a somewhat higher formation temperature of around 45 K. Taking the $Ar/CO = (0.187 \pm 0.091)$‰ ratio into account, Mousis et al. (2018) then suggested a further refined crystalline ice model requiring multiple layers of reconfigured ices.

Table 2 yields $N_2/CO = (2.9 \pm 1.2) \cdot 10^{-2}$ in the bulk of the nucleus for the 2015 May period, which is about five times higher than the value derived in Rubin et al. (2015a) for the October 2014 period listed above. This result hints at an even lower formation temperature, closer to 20 K for the amorphous ice case. Such a temperature would also be consistent with the temperature range derived independently by Taquet et al. (2016) from the measured $O_2/H_2O = (3.80 \pm 0.85) \times 10^{-2}$ in comet 67P/C-G by Bieler et al. (2015), which is compatible within error bars with the value derived here $O_2/H_2O = (3.1 \pm 1.1) \times 10^{-2}$ from Table 2.

Elemental abundances in the volatile species can be derived for a suite of comets. Fig. 4 shows a comparison of the major elements H, C, N, and S normalized to O in cometary volatile species for both, Oort Cloud Comets (OCCs) and JFCs. While there is some scatter in the observations, i.e. the number of species observed is different from comet to comet, some conclusions can still be drawn. Hydrogen and oxygen are the two major elements in the volatile species, given that water is the main component in cometary ices. The third most abundant element is carbon, originating mostly from CO and CO_2, although its relative abundance varies by more than a factor of 10, which is in line with the very variable CO abundances within comets (Dello Russo et al. 2016). Trends are difficult to assess as perihelion distances, which are a measure of peak heating, and heliocentric distances during the times of observation vary amongst comets (A'Hearn et al. 2012). The same applies to the number of perihelion passages a comet has undergone in the past. Furthermore, the abundance of CO_2 is unknown for many comets, but may contribute substantially to the C-content in the ices. The abundance of S-bearing and N-bearing species is also quite

Table 4. Elemental H, C, N, and O abundances in the ice (Table 3) and dust (Bardyn et al. (2017) and Fray et al. (2016) with estimated H/Si) in comet 67P/Churyumov-Gerasimenko per silicon atom for dust-to-ice ratios of 1 and 3 by weight.

Element	Dust	Volatiles (D/I = 1)	Volatiles (D/I = 3)	Combined (D/I = 1)	Combined (D/I = 3)
H/Si	$5.4^{+5.7}_{-2.6}$	$18.5^{+0.3}_{-0.3}$	$6.2^{+0.1}_{-0.1}$	24^{+6}_{-3}	12^{+6}_{-3}
C/Si	$5.4^{+9.2}_{-4.8}$	$0.87^{+0.27}_{-0.26}$	$0.29^{+0.09}_{-0.09}$	$6.3^{+9.2}_{-4.8}$	$5.7^{+9.2}_{-4.8}$
N/Si	$0.19^{+0.37}_{-0.19}$	$0.090^{+0.028}_{-0.028}$	$0.030^{+0.009}_{-0.009}$	$0.28^{+0.37}_{-0.19}$	$0.22^{+0.37}_{-0.19}$
O/Si	$5.4^{+8.5}_{-4.1}$	$10.5^{+0.6}_{-0.6}$	$3.5^{+0.2}_{-0.2}$	16^{+9}_{-4}	$8.9^{+8.5}_{-4.1}$

Table 5. Distribution of H, C, N, O, and Si by number in grains and ice. Based on Table 3 for two dust-to-ice ratios inside the nucleus, D/I = 1 and D/I = 3 by weight.

Element	D/I = 1		D/I = 3	
	Dust (per cent)	Ice (per cent)	Dust (per cent)	Ice (per cent)
H	22^{+18}_{-8}	78^{+18}_{-8}	46^{+26}_{-12}	54^{+26}_{-12}
O	34^{+35}_{-17}	66^{+34}_{-17}	61^{+37}_{-18}	39^{+37}_{-18}
C	86^{+14}_{-11}	14^{+20}_{-11}	95^{+5}_{-4}	5^{+8}_{-4}
N	68^{+32}_{-23}	32^{+44}_{-23}	86^{+14}_{-12}	14^{+24}_{-12}
Si	100	0	100	0

variable amongst comets, with the caveat that there is very little information available on S-bearing species for JFCs apart from 67P/C-G. None the less, this supports A'Hearn et al. (2012) who found no systematic differences between the OCCs and JFCs.

The elemental abundances in the bulk of comet 67P/C-G depend on both the dust-to-ice (D/I) ratio (by weight) and the elemental composition in both the dust and the gas (cf. Table 3). Table 4 lists the ratios of the elements abundantly found in the volatile species relative to Si, which is typically found in the refractory material. The contributions have been obtained separately for the dust, the volatiles, and the nucleus total for two representative D/I ratios. Estimated dust-to-gas (D/G) ratios in the coma based on ROSINA measurements have been presented by Hansen et al. (2016) and Läuter et al. (2019) and yield a D/I ratio of around 1, even when including some 20 per cent of dry dust backfall (Keller et al. 2017), which may be missing in the D/G ratio measured in the coma.

For comparison, we also investigated a higher D/I ratio of 3, within the range of the $(D/I = \ )\ D/G = 4 \pm 2$ reported by Rotundi et al. (2015). Even higher D/I ratios (cf. Fulle et al. 2018), which would be associated with a higher percentage of backfall of dry dust, can easily be derived from the numbers given in Table 4. The most prominent differences when changing the D/I ratio are expected in the H/Si and O/Si ratios, given that water is the main component in the cometary ices.

As a consequence of these numbers, the distribution of the different elements amongst the dust and the ice could also be computed. Table 5 shows that the majority of the hydrogen atoms resides in the ices. However, this changes for high D/I ratios. A similar picture arises for oxygen, whereas carbon and nitrogen seem to be predominantly in the refractories. These results are consistent with earlier findings at OCC 1P/Halley by Geiss (1987), who assumed that the dust-to-gas ratio in the coma reflected the dust-to-ice ratio in the nucleus, i.e. $D/G = D/I = 0.5$ based on McDonnell et al. (1986). The inferred high abundance of C-bearing species in the refractory material of 67P/C-G derived from COSIMA measurements (Fray et al. 2016; Bardyn et al. 2017) are in agreement with measurements obtained at comet 1P/Halley (Jessberger et al. 1988). However, the macromolecular matter observed by COSIMA and the zoo of (semi-)volatile organic molecules detected by ROSINA (Altwegg et al. 2017b; Schuhmann et al. 2019a,b) still leaves room for a suite of complex organics to fill the gap between the two. Whether such a continuum exists is still an open question and could further affect the distribution of the elements H, O, C, and N between dust and ice.

The combined elemental abundance ratios from Table 4 (cf. Bardyn et al. 2017; Fray et al. 2017) can also be compared to other objects in the Solar system. Fig. 5 reproduces the plot by Geiss (1987) with the addition of the comet 67P/C-G. Similar to 1P/Halley, near-solar O/Si and C/Si ratios were found in 67P/C-G and N/Si was depleted compared to solar. D/I ratios inside the nucleus versus in the coma are still a matter of debate, fuelled by the redisposition of material at 67P/C-G (Rubin et al. 2014; Thomas et al. 2015). Both comets hence display consistent ratios considering the error bars and the uncertainty in the D/I ratio, the latter impacting mostly H/Si and O/Si as discussed earlier. Meteorites, and even more so the Earth, show higher degrees of devolatilization. In particular, both C/Si and N/Si are much lower compared to both the Sun and comets.

The depletion of H/Si in the ices of the comet compared to the Sun was expected due to the high volatility of H (Geiss 1987). The uncertainty of N-abundance in 1P/Halley was larger than for the other elements, hence two estimates were provided. The *Rosetta* mission obtained a better estimate of the total volatile *N*-abundance through the detailed quantification of the amount of N_2 (Rubin et al. 2015a). The major contributor to the elemental abundance of nitrogen in the volatile species is NH_3, followed by N_2 and HCN, the latter including HNC. Several additional N-bearing species have been identified, though the N-depletion in comet 67P/C-G, as shown in Fig. 5, is still comparable to earlier measurements at comet 1P/Halley.

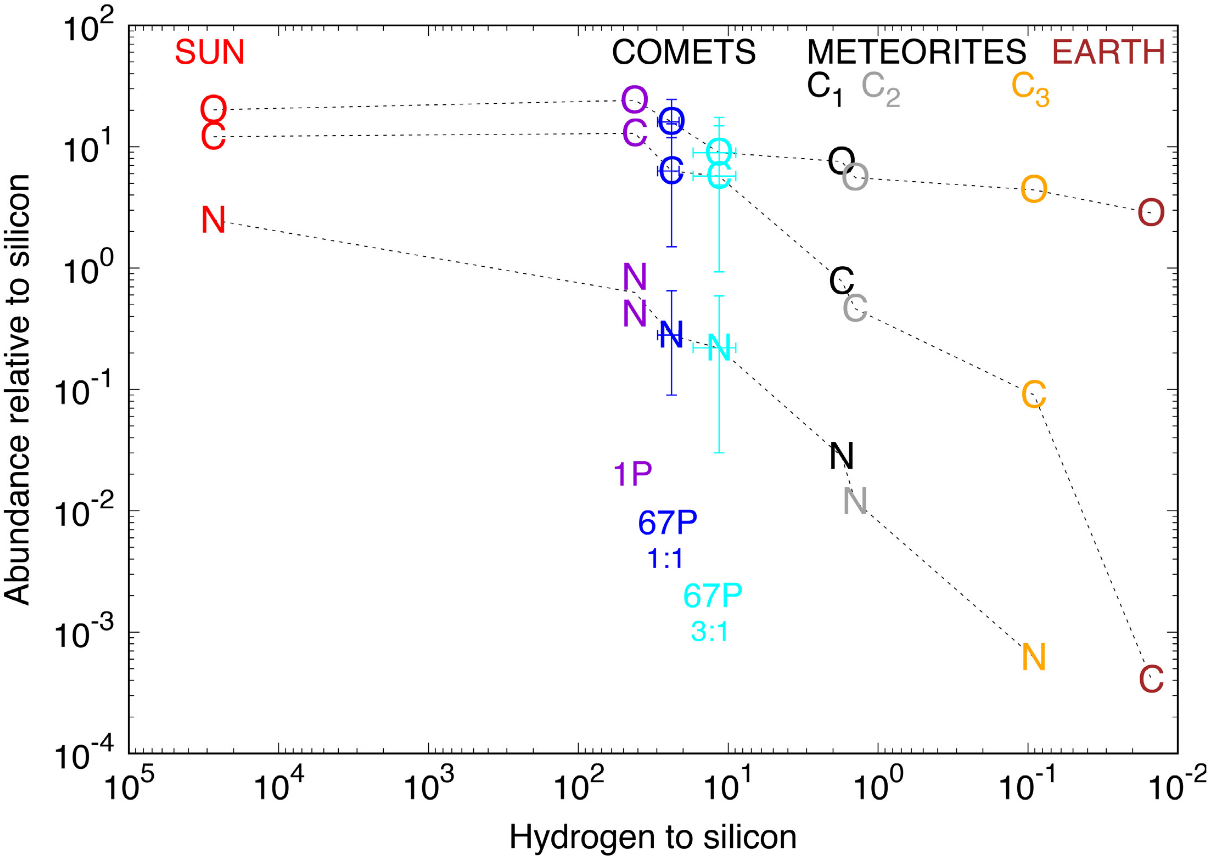

Figure 5. Elemental abundances of H, C, N, and O relative to Si in the solar nebula (red; Anders & Ebihara 1982), comet 1P/Halley [purple, for D/I = 0.5 and two estimates for N from Balsiger et al. (1986) and Allen et al. (1987); Geiss (1987)], comet 67P/C-G (for D/I = 1 in blue and D/I = 3 in turquoise), carbonaceous chondrites [C_1 in black, C_2 in grey, and C_3 in orange; Kerridge (1985)], and an estimate of the Earth's crust and mantle [brown; Larimer (1971), Wänke (1981), and Wänke, Dreibus & Jagoutz (1984)]. See Table 4 for data on 67P/C-G and Geiss (1987) for the others.

Other differences between OCC 1P/Halley and JFC 67P/C-G can be explained by the distinct D/I ratios and the lower CO abundance derived for the ices of 67P/C-G in comparison with the >10 per cent of CO with respect to water at 1P/Halley (Eberhardt 1999; Rubin et al. 2011). Furthermore, their different dynamic histories may have led to additional fractionation, as 67P/C-G was subjected to heating during the transition through the Centaur stage (Guilbert-Lepoutre et al. 2016).

Potential differences between the comet families, JFCs versus OCCs, have also been discussed based on the assumption that the different families formed in two distinct zones (Duncan & Levison 1997). However, later results based on D/H measurements [cf. Altwegg et al. (2017a) and references therein] in the water of a suite of OCCs and JFCs support the theory that the comets in both families may have formed over a wide range of overlapping heliocentric distances before being scattered to where they are found today (Brasser & Morbidelli 2013). Based on the results shown in Fig. 5, Geiss (1987) concluded that comets are regular members of our Solar system and that they must have preserved the original material better than other objects. This certainly also holds for JFC 67P/C-G.

ACKNOWLEDGEMENTS

ROSINA would not have produced such outstanding results without the work of the many engineers, technicians, and scientists involved in the mission, in the *Rosetta* spacecraft team, and in the ROSINA instrument team over the last 20 yr, whose contributions are gratefully acknowledged. *Rosetta* is an ESA mission with contributions from its member states and NASA. We acknowledge herewith the work of the whole ESA Rosetta team.

Work at the University of Bern was funded by the State of Bern, the Swiss National Science Foundation (SNSF, 200021_165869 and 200020_182418), the Swiss State Secretariat for Education, Research and Innovation (SERI) under contract number 16.0008–2, and by the European Space Agency's PRODEX Programme. MND acknowledges the financial support of the SNSF Ambizione grant 180079, the Center of Space and Habitability (CSH) Fellowship, and the International Astronomical Union (IAU) Gruber Foundation Fellowship. SFW acknowledges the financial support of the SNSF Eccellenza Professorial Fellowship PCEFP2_181150. JDK acknowledges support by the Belgian Science Policy Office via PRODEX/ROSINA PEA 90020. JHW acknowledges Jet Propulsion Laboratory (JPL) subcontract NAS703001TONMO710889. SAF acknowledges JPL contract 1496541. Work at MPS was funded by the Max-Planck Society and the

Bundesministerium fuer Wirtschaft und Energie (BMWi) under contract 50QP1302. Work at the University of Michigan was supported by contracts JPL 1266313 and JPL 1266314 from the US Rosetta Project.

REFERENCES

A'Hearn M. F. et al., 2012, ApJ, 758, L29

Allen M., Delitsky M., Huntress W., Yung Y., Ip W.-H., 1987, A&A, 187, 502

Altwegg K. et al., 2016, Sci. Adv., 2, e1600285

Altwegg K. et al., 2017a, Phil. Trans. R. Soc. A (Math. Phys. Eng. Sci.), 375, 1

Altwegg K. et al., 2017b, MNRAS, 469, S130

Anders E., Ebihara M., 1982, Geochim. Cosmochim. Acta, 46, 2363

Balsiger H. et al., 2015, Sci. Adv., 1, e1500377

Balsiger H. et al., 2007, Space Sci. Rev., 128, 745

Balsiger H. et al., 1986, Nature, 321, 330

Bar-Nun A., Notesco G., Owen T., 2007, Icarus, 190, 655

Bardyn A. et al., 2017, MNRAS, 469, S712

Bibring J. P. et al., 2015, Science, 349, 493

Bieler A. et al., 2015, Nature, 526, 678

Biver N. et al., 1999, AJ, 118, 1850

Biver N. et al., 2007, Planet. Space Sci., 55, 1058

Biver N. et al., 2014, A&A, 566, L5

Biver N. et al., 2019, A&A

Biver N. et al., 2016, A&A, 589, A78

Bockelée-Morvan D. et al., 2015, Space Sci. Rev., 197, 47

Bockelée-Morvan D. et al., 2016, MNRAS, 462, S170

Bockelée-Morvan D., Crovisier J., Mumma M. J., Weaver H. A., Keller H. U., Weaver H. A., 2004, in Festou M. C., Keller H. U., Weaver H. A., eds, Comets II. Univ. Arizona Press, Tucson, AZ, p. 391

Bockelée-Morvan D. et al., 2000, A&A, 353, 1101

Bodewits D. et al., 2016, AJ, 152, 130

Böhnhardt H., Mumma M. J., Villanueva G. L., DiSanti M. A., Bonev B. P., Lippi M., Käufl H. U., 2008, ApJ, 683, L71

Bonev B. P., Mumma M. J., Radeva Y. L., DiSanti M. A., Gibb E. L., Villanueva G. L., 2008, ApJ, 680, L61

Brasser R., Morbidelli A., 2013, Icarus, 225, 40

Brownlee D. et al., 2006, Science, 314, 1711

Calmonte U. et al., 2016, MNRAS, 462, S253

Calmonte U. M., 2015, PhD thesis, Universität Bern

De Keyser J. et al., 2017, MNRAS, 469, S695

Dello Russo N., Kawakita H., Vervack R. J., Weaver H. A., 2016, Icarus, 278, 301

Dhooghe F. et al., 2017, MNRAS, 472, 1336

DiSanti M. A., Bonev B. P., Magee-Sauer K., Russo N. D., Mumma M. J., Reuter D. C., Villanueva G. L., 2006, ApJ, 650, L470

Duncan M. J., Levison H. F., 1997, Science, 276, 1670

Eberhardt P., 1999, Space Sci. Rev., 90, 45

Feldman P. D. et al., 2015, A&A, 583, A8

Feldman P. D. et al., 1987, A&A, 187, 325

Feldman P. D., Weaver H. A., Burgh E. B., 2002, ApJ, 576, L91

Fougere N. et al., 2016a, A&A, 588, A134

Fougere N. et al., 2016b, MNRAS, 462, S156

Fougere N., Combi M. R., Rubin M., Tenishev V., 2013, Icarus, 225, 688

Fray N. et al., 2016, Nature, 538, 72

Fray N. et al., 2017, MNRAS, 469, S506

Fulle M. et al., 2018, MNRAS, 482, 3326

Furuya K., van Dishoeck E. F., Aikawa Y., 2016, A&A, 586, A127

Fuselier S. A. et al., 2015, A&A, 583

Gasc S. et al., 2017a, MNRAS, 469, S108

Gasc S. et al., 2017b, Planet. Space Sci., 135, 64

Geiss J., 1987, A&A, 187, 859

Glassmeier K. H., Boehnhardt H., Koschny D., Kuhrt E., Richter I., 2007, Space Sci. Rev., 128, 1

Goesmann F. et al., 2015, Science, 349, aab0689

Graf S. et al., 2004, J. Geophys. Res. Planet., 109, E07S08

Guilbert-Lepoutre A., Rosenberg E. D., Prialnik D., Besse S., 2016, MNRAS, 462, S146

Hansen K. C. et al., 2016, MNRAS, 462, S491

Hässig M. et al., 2015, Science, 347, aaa0276

Herbst E., van Dishoeck E. F., 2009, ARA&A, 47, 427

Hoang M., et al., 2017, A&A, 600, A77

Jessberger E. K., Christoforidis A., Kissel J., 1988, Nature, 332, 691

Keller H. U. et al., 2017, MNRAS, 469, S357

Kerridge J. F., 1985, Geochim. Cosmochim. Acta, 49, 1707

Kim Y.-K., et al., 2005, National Institute of Standards and Technology, doi:10.18434/T4KK5C

Kissel J. et al., 2007, Space Sci. Rev., 128, 823

Kobayashi H. et al., 2010, A&A, 509, A80
Larimer J. W., 1971, Geochim. Cosmochim. Acta, 35, 769
Läuter M., Kramer T., Rubin M., Altwegg K., 2019, MNRAS, 483, 852
Le Roy L. et al., 2015, A&A, 583, A1
Lectez S., Simon J. M., Mousis O., Picaud S., Altwegg K., Rubin M., Salazar J. M., 2015, ApJ, 805, L1
Lien D. J., 1990, ApJ, 355, 680
Marschall R. et al., 2017, A&A, 605, A112
Marshall D. W. et al., 2017, A&A, 603, A87
Marty B. et al., 2017, Science, 356, 1069
Mattauch J., Herzog R. F.K., 1934, Z. Physik, 9, 786
McDonnell J., Kissel J., Grün E., Grard R., Langevin Y., Olearczyk R., Perry C., Zarnecki J., 1986, ESLAB Symp. Exploration Halley's Comet
McKeegan K. D. et al., 2006, Science, 314, 1724
Mousis O. et al., 2018, ApJ, 865, L11
Nevejans D., Neefs E., Kavaias S., Merken P., Van Hoof C., 2002, Int. J. Mass Spectrom., 215, 77
Paganini L., Mumma M., Villanueva G., DiSanti M., Bonev B., Lippi M., Boehnhardt H., 2012, ApJ, 748, L13
Remijan A. J. et al., 2006, ApJ, 643, L567
Rotundi A. et al., 2015, Science, 347, aaa3905
Rubin M. et al., 2015a, Science, 348, 232
Rubin M. et al., 2018, Sci Adv, 4, eaar6297
Rubin M., Altwegg K., van Dishoeck E. F., Schwehm G., 2015b, ApJ, 815, L11, https://iopscience.iop.org/article/10.1088/2041-8205/815/1/L11/meta
Rubin M., Fougere N., Altwegg K., Combi M. R., Le Roy L., Tenishev V. M., Thomas N., 2014, ApJ, 788, 168
Rubin M., Tenishev V. M., Combi M. R., Hansen K. C., Gombosi T. I., Altwegg K., Balsiger H., 2011, Icarus, 213, 655
Schroeder I., et al., 2018, A&A, 10.1051/0004-6361/201833806
Schuhmann M. et al., 2019a, A&A, 10.1051/0004-6361/201834666
Schuhmann M. et al., 2019b, ACS Earth Sp. Chem., 10.1021/acsearthspacechem.9b00094
Schwehm G., Schulz R., 1999, Space Sci. Rev., 90, 313
Sierks H. et al., 2015, Science, 347, aaa1044
Taquet V., Furuya K., Walsh C., van Dishoeck E. F., 2016, MNRAS, 462, S99
Tenishev V., Combi M., Davidsson B., 2008, ApJ, 685, 659
Thomas N. et al., 2015, A&A, 583, A17
Tzou C.-Y., 2017, PhD thesis, Univ. Bern
Wänke H., 1981, Phil. Trans. R. Soc. Lond. A, 303, 287
Wänke H., , Dreibus G., Jagoutz E., 1984, in Kroener A., Hanson G. N., Goodwin A. M.eds, Archaean Geochemistry. Springer, Berlin, Heidelberg, p. 1
Wright I. P., Sheridan S., Barber S. J., Morgan G. H., Andrews D. J., Morse A. D., 2015, Science, 349, aab0673
Wurz P. et al., 2015, A&A, 583, A22, 1–9
Zakharov V. V., Crifo J. F., Rodionov A. V., Rubin M., Altwegg K., 2018, A&A, 618, A71

This paper has been typeset from a Microsoft Word file prepared by the author.